Chapter 4

Investigation of Laser Pulse-induced Calculus Damage Mechanism by a High-speed Camera

Jian J. Zhang, Rongwei J. Xuan and
Thomas Hasenberg

Additional information is available at the end of the chapter

http://dx.doi.org/10.5772/intechopen.69981

Abstract

Even though laser lithotripsy has become the most popular treatment choice for kidney stone disease, the mechanism calculus disintegration by laser pulse remains unclear. This is due to the multiple physical/chemical processes involved in laser pulse-caused calculus damage and their sub-microsecond timescales. A high-speed camera with a frame rate up to 1 million frames per second (fps) was employed in this study. The results revealed the cavitation bubble dynamics (oscillation and center of bubble movement) by Ho- and Tm-laser pulses at a different energy level and pulse width. Besides, fiber-tip degradation, damage, or burn-back is a common problem during the ureteroscopic laser lithotripsy procedure to treat urolithiasis. The results suggested that using a high-speed camera and the Schlieren method to visualize the shock wave provided valuable information about time-dependent acoustic energy propagation and its interaction with cavitation, the fiber tip, and calculus. And lastly, calculus migration is a common problem during ureteroscopic laser lithotripsy procedure to treat urolithiasis. In this investigation, calculus retropulsion was studied using a suspended pendulum in water to get rid of the friction. The results suggested that using the pendulum model to eliminate the friction improved sensitivity and repeatability of the experiment.

Keywords: calculus, cavitation, bubble, dynamics, shock wave, oscillation, high-speed camera, fiber burn-back, retropulsion, laser lithotripsy

1. Introduction

1.1. Cavitation bubble dynamics

Kidney stone diseases are crystallized solids, for example, kidney/ureter/bladder/urethra calculi or uroliths, which crop up in the urinary tract. The patient suffers acute ache and discomfort. Urolithiasis is the third largest disease in urology following urinary tract infection and prostate condition. It affects 10% of the US population at a significant recurrence of ~50% [1–3]. Shock wave lithotripsy (SWL) and the ureteroscopic laser lithotripsy (URS) are the top two most frequent treatment options in the USA for the treatment of ureteral stones [4, 5]. The review investigation in Ref. [6] concluded better stone-free rates (SFRs) for renal stones <15 mm for URS compared with SWL. Even though laser lithotripsy has become the most popular treatment choice for kidney stone disease, the mechanism of calculus disintegration by laser pulse remains unclear. This is due to the multiple physical/chemical processes involved in laser pulse-caused calculus damage and their sub-microsecond timescales (as listed in **Table 1**) and their timescales are very short (down to sub-microsecond level).

For laser lithotripsy, the laser pulse-induced impact by energy flow can be summarized in **Figure 1** as follows: [7]

- Photon energy in the laser pulse that includes the laser pulse train propagating through the delivery fiber and passing through the fiber tip (the fiber tip is typically uncoated and there will be a Fresnel reflection loss).
- Photon absorption that generates heat in the water liquid and vapor (resulting in superheated water exceeding 100°C or a plasma effect with temperatures up to thousands of degree accompanied by light emission).
- Shock wave generation (at the initial injection of the laser pulse into the water. This is a Bow shock effect that results in an initial strong disturbance but dampens to a regular acoustic wave after traveling a fraction of a millimeter)

Effects	Thermal (heat up, vaporization, melt)	Light emission (plasma, super-heated water and stone particle, sonoluminescence)	Shock wave (supersonic, pressure shock)	Bubble dynamics (oscillation, center propagation, Acoustic wave)	Break (Chemical/ mechanical, fragmentation/dusting, spallation)	Kinetic move (debris ejection, retropulsion...)
Symbol						

Table 1. Physical and chemical processes during laser pulse-induced calculus damage [7].

http://dx.doi.org/10.5772/intechopen.69981

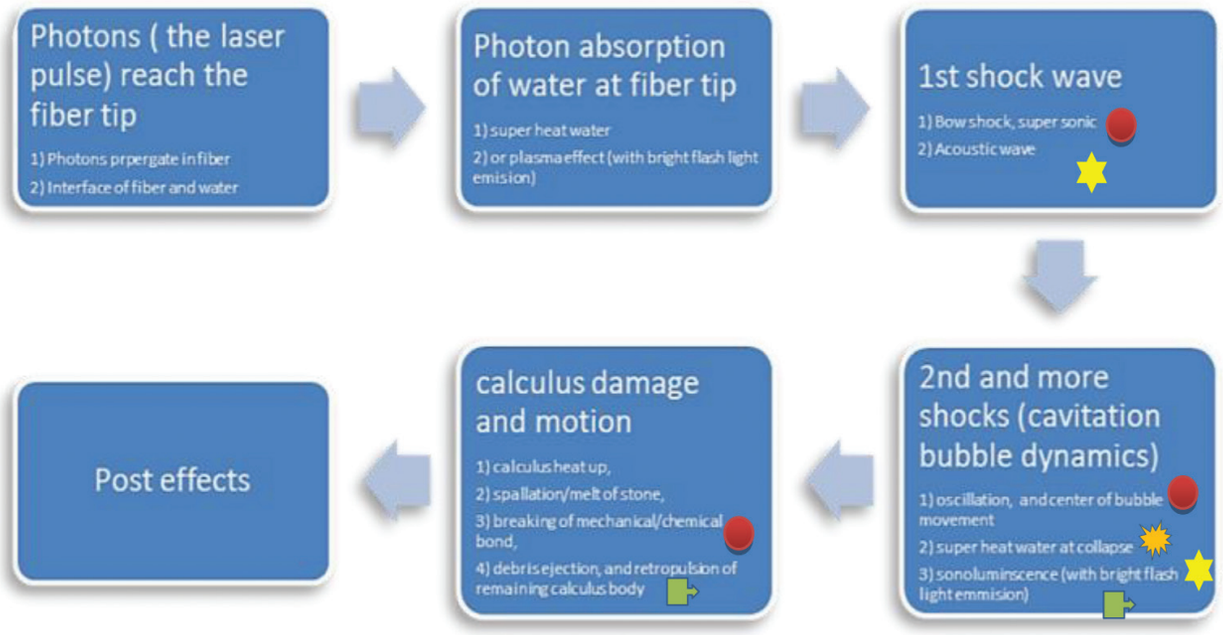

Figure 1. The energy flow block diagram of the laser pulse-induced calculus damage.

- Cavitation bubble dynamics (these include the cavitation bubble oscillation, the translational movement of the bubble represented by the center of bubble, the then super-heated water at the bubble collapse, the light emission by sonoluminescence, the shock wave created at the collapses of the cavitation bubble, etc.).
- Calculus damage and motion:
  i. Spallation: calculus damage through heating as the calculus rapidly absorbs the laser energy, thereby imposing a stress wave on the calculus surface. The magnitude of the stress wave and the temperature rise is proportional to absorption coefficient of the phantom; the high magnitude of the stress wave in calculus can cause spallation process;
  ii. Micro-explosion: the explosion of interstitial water content within the pores of the calculus;
  iii. Melt: direct absorption of laser photons by calculus that causes a temperature increase that exceeds the melting point of the calculus;
  iv. Breaking: breaking of the mechanical or chemical bond between the calculus molecules;
  v. Motion: includes debris ejection and retropulsion [8] of the remaining calculus body.
- Post effect (thermal dissipation across the calculus and through the surrounding fluids; debris spreading out by the acoustic waves, etc.).

Cavitation bubble [9–16] dynamics are the centerpiece of the physical processes that link the whole energy flow chain from laser pulse to calculus damage.

In this study, cavitation bubble dynamics have been investigated by utilizing a high-speed camera and a needle hydrophone. We keep the following three questions in mind when performing

this investigation: (1) What are the differences in the characteristics of the bubble dynamics between a short pulse and a long pulse for Ho:YAG laser? A reduction of retropulsion and reduced fiber burn-back has been demonstrated by employing long-pulse modes in Ho:YAG lasers in contrast to short-pulse modes [17]. Several Ho:YAG laser vendors offer variable pulse option including the AMS StoneLight™ 30, pulse with a range from 150 to 800 μs. Indeed, it would be interesting to investigate the cavitation bubble dynamics as a function of pulse width; (2) there has been a dispute as to whether or not a cavitation bubble forms during lithotripsy when the fiber tip is in contact with the surface of the calculus. This contact mode is a common practice during treatment of urolithiasis and can be studied with a high-speed camera; (3) although Ho:YAG lithotripter is the benchmark for laser lithotripsy, the cavitation bubble dynamics and transient pressure level of other laser sources including the Q-switched (QS) Tm:YAG laser [18, 19] were also investigated. The study revealed the cavitation bubble dynamics (oscillation and center of bubble movement) and transient pressure levels of the Ho:YAG and Tm:YAG laser pulses at different energy levels and pulse widths. A more detailed investigation of the relationship between cavitation bubble dynamics and calculus damage (fragmentation/dusting) will be conducted in a future study.

1.2. Fiber-tip damage mechanism

The review investigation in Ref. [6] concluded better stone-free rates for renal stones <15 mm for URS compared with SWL. However, the delivery fiber employed in URS encountered distal-end burn-back [20–23].

As shown in **Figure 2** [11], fiber-tip (distal-end) degradation/damage/burn-back is a constant issue during the URS treatment of kidney stone disease. Fiber-tip damage leads to a decreased transmittance of laser power, which could lead to significant decrease of stone comminution. On certain occasion, the fiber-tip burn-back is so much that the degraded fiber tip will consume a lot of the laser power, which can lead to such a high temperature that exceeds the melting temperature of the fiber-cladding layer or polymer jacket. Although, it is a common

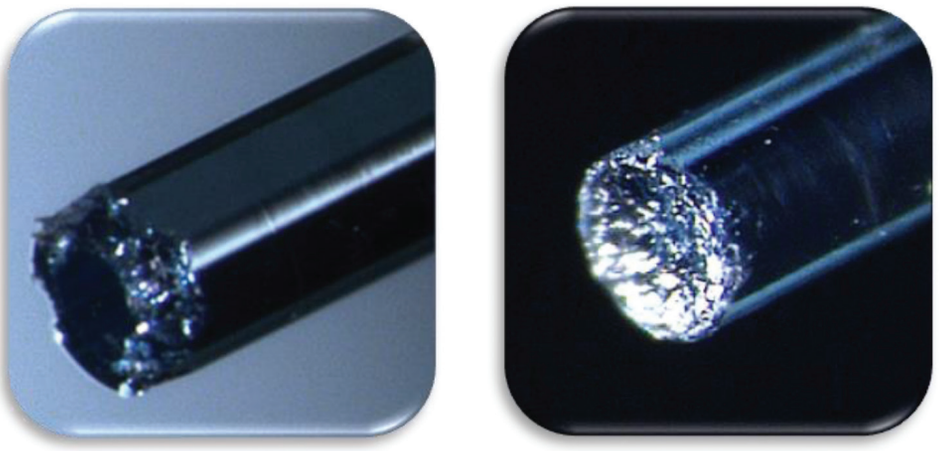

Figure 2. Samples of degraded fiber-end (burn-back).

http://dx.doi.org/10.5772/intechopen.69981

sense that the bigger the laser energy density at the fiber tip, the faster the tip deterioration, the burn-back mechanism of the fiber tip remains unclear.

Fiber-tip damage/degradation/burn-back mechanism is a complex subject due to its numerous physical phenomena, for example, sonic shock waves, self-focusing of the laser beam, and transient thermal surge, and so on. It covers three areas of degradation mechanisms: (1) Mechanical: shock wave and debris impulsion; (2) Thermal: heating/liquidating of material, transient thermal surge because of the absorption of self-focusing laser beam by the microstructure of the fiber-tip surface material; (3) Optical: photoionization or plasma [24] as shown in **Figure 3**.

In this investigation, the fiber-tip damage was studied by visualization of the pressure wave, cavitation bubble dynamics, and ejected phantom stone debris using a high-speed camera and the Schlieren technique. A high-speed camera is a great device to study the relationship of the laser pulse with the phantom stone, as well as the recoil motion [8]. The principal chromophore of the 2.01-μm Holmium laser is water, which is critical for fragmentation of the calculus during laser lithotripsy [19]. The shock wave [9, 10, 12–14] that the laser pulse generates is a disturbance wave that travels faster than sound and is one of the mechanical causes of the fiber-tip damage (**Figure 2**). Because of the transparency of water liquid, pressure wave imaging inside water is not as straightforward. However, the Schlieren method can reveal the acoustic wave inside water, just like an X-ray which can reveal the invisible pressure variation inside a transparent matter. In this technique, a knife edge is placed at a focal spot to reduce the number of rays that do not interact with the acoustic field to reveal those that do interact; in physical optics terms, the Schlieren technique converts the phase information into an intensity image.

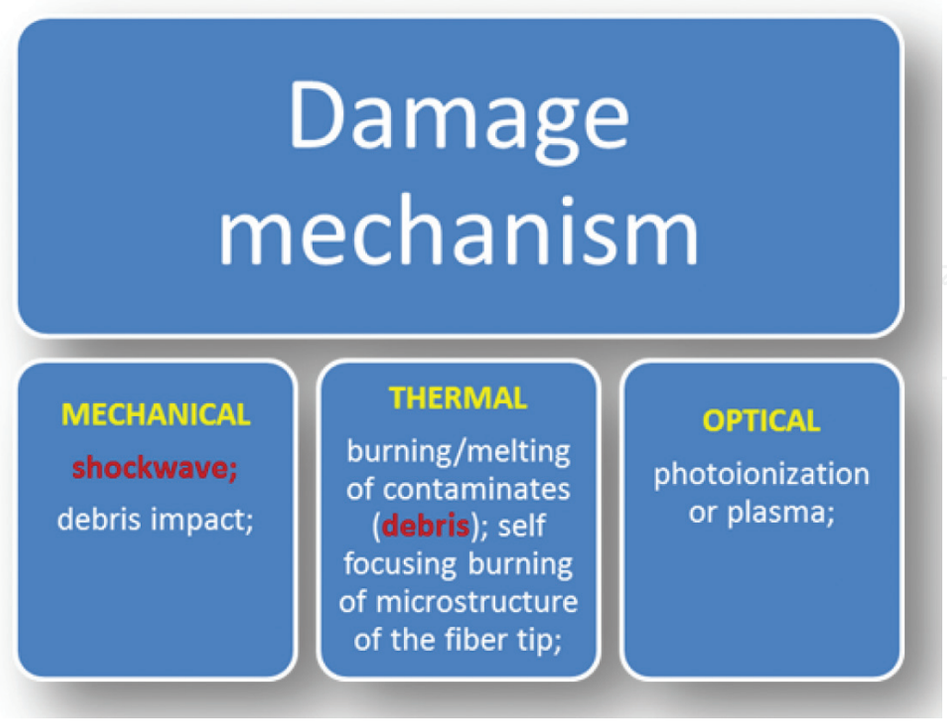

Figure 3. The degradation mechanism of the fiber tip (the items in red are studied in this investigation).

A commercially available pulsed Ho:YAG laser at 2.13 with a 365-μm core diameter fiber impinging on calculus phantoms (Plaster of Paris, white gypsum cement, 10-mm cube) was employed to simulate the URS process. Laser power-caused pressure wave, cavitation bubble dynamics, and calculus particles scattering were videotaped by a high-speed camera with 10,000–930,000 frames per second (fps). The pressure wave is captured by the Schlieren method. The contribution of ejected stone particles in fiber-tip degradation is also investigated. The study concluded that using a high-speed camera combining with the Schlieren technique is a powerful tool to study the movement of the pressure wave and its relationship with bubble dynamics and stone damage. More study in pressure wave shaping by the geometric shape of the fiber tip and the detailed mechanisms of shock waves, cavitation bubble dynamics, and calculus debris ejection will be investigated in a future study.

1.3. Calculus migration/retropulsion

During the treatment of urolithiasis, the urinary calculus is subjected to retropulsion forces induced by the combined effects of ablated particle ejection, interstitial water vaporization, and bubble dynamics [25–27]. Therefore, because of the retropulsion, the stone has moved away from the fiber tip. This can cause longer procedure time because of additional steps of finding the dislocated stone and repositioning the fiber tip to it. Recoil motion investigations in the past revealed the relation between retropulsion displacement and laser power, frequency, and fiber core size [28–31]. Recoil motion is proportional to the laser power and the fiber core size. Furthermore, another research claimed that the recoil motion decreased with a longer laser pulse without compromising dusting effectiveness significantly [32].

The amplitude of stone recoil motion (retropulsion) during kidney stone treatment depends mainly on the power source or instrument. The pneumatic or electrohydraulic lithotripters cause a much bigger recoil motion than laser lithotripters [30, 33–34]. Nevertheless, the laser lithotripters can cause noticeable dislocation of the stone during the procedure. A few investigations of the URS treatment of upper ureteral calculi have revealed that the main reason for calculus-free failures can be due to recoil motion and less frequently to inability to track or seek the stones [35–37]. Recoil-dislocated calculus could lead to longer operation period, the necessity for another process to deal with recoiled parts and as such reduced stone-free level. The stone recoil motion results in additional patient morbidity and health-care expenses [30, 33]. Besides, left-behind stone debris can act as a seed for calculus growing back, renal colic, and persistent infection.

The previous studies on stone retropulsion often employed a holder, like a test tube or a "V" shape groove. These approaches, however, have shown large uncertainty and low accuracy, most likely due to the friction between the stone phantom and the holder on which the stone phantom stationed. For instance, stone phantoms (Plaster of Paris, 10-mm cube) were employed to simulate the URS process, with the previous methodology resulted in <0.5-mm entire recoil movement (either with a "V" grove or a test tube). When scaling down the stone size to 5-mm cube (1/8 in volume), the recoil movement was very unpredictable. Our earlier study of recoil movement on a 5-mmcube resulted in a 59% standard deviation [38], for example, a peak-to-peak recoil movement range of ~3–10 times as much.

Sroka et al. [39] employed a sphere-shaped lead ball hung with a nylon string to investigate the recoil motion in URS by a standard CCD camera. In this investigation, a calculus phantom in water formed a pendulum, and the phantom recoil motion is studied using this approach to get rid of any friction that could occur if a holder was employed to host the calculus. This method mostly decreased the migration variation of recoil motion in URS. Furthermore, a high-speed camera was used to study the movement of the calculus which covered zero-order (displacement), first-order (speed), and second-order (acceleration) dynamics. This study employed a commercially available pulsed Ho:YAG laser at 2.1- and 365-μm core fiber, and calculus phantoms (Plaster of Paris, 10 × 10 × 10 mm^3 cube) to mimic laser lithotripsy procedure.

2. Experimental method and setup

2.1. Cavitation bubble dynamics

2.1.1. Fiber

Figure 4 shows a picture of SureFlex™ fibers, Model S-LLF273/365, 273/365-μm core diameter fibers (S-LLF273/365 SureFlex Fibre, Boston Scientific Corp., San Jose, CA, USA) that are used in the test of this study.

2.1.2. Calculus phantom

Calculus phantoms made of Plaster of Paris gypsum employed as tissue phantom for human calculi (UtralCal®30, United States Gypsum Company, Chicago, IL, USA), were broadly utilized for URS investigations by other investigators [40]. The calculus phantoms are made by mixing gypsum powder (500 g) with distilled water (0.23 l) and followed by curing for more than 3 h (preferred overnight). The gypsum was cast to have a dimension of 10-mm cube as indicated in **Figure 5**. The average weight of the stone phantom is 1.8 g, and with a tensile strength of 2 MPa, which is similar to the tensile strength of a human struvite (0.1–3.4 MPa) [41].

Figure 4. Picture of SureFlex™ 273- and 365-μm fibers.

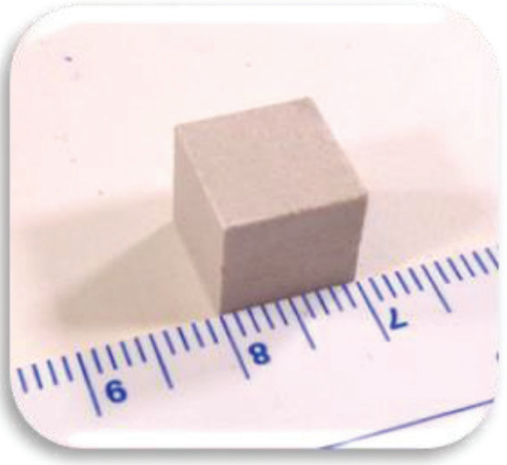

Figure 5. 10 × 10 × 10 mm^3 calculus phantom.

2.1.3. Laser system

The laser systems utilized in this study included a pulsed Ho:YAG laser at 2.13 μm, Holmium 30 W (StoneLight™ 30, American Medical Systems, San Jose, CA, USA), with pulse energy from 0.5 up to 3.0 J, and pulse width from 150 up to 800 μs, as well as a Q-switched Tm:YAG laser at 2.01 μm with pulse energy of ~0.02 J. **Figure 6** shows a temporal pulse structure diagram of StoneLight™ 30 Ho:YAG laser with the pulse duration (τ_p) of ~240 μs. This magnitude of pulse duration is known to generate the necessary photothermal effect of fragmenting the stones [42].

A lab-constructed Q-switched Tm:YAG laser (2.01 μm) was used for this investigation, as indicated in **Figure 7**. The gain medium Tm:YAG is energized by laser diode pumping beam from a laser diode stack via a delivery system. An optical focusing glass is employed to compensate the strong thermal lens of Tm:YAG medium to sustain the stability of the resonator cavity. Besides, a lab-built acoustic Q-switch is oriented within the resonator to manipulate the output beam in a Q-switched manor. The laser has a frequency from 1 up to 2 kHz and pulse energy of 20 mJ at the distal end of the beam delivery fiber. Singular light pulse at the far end of the delivery fiber can be dispatched by an extra-cavity shutter in between the output window (OC) of laser resonator and the light-focusing optics system. **Figure 8** displays a light pulse with a pulse length (τ_p) of 750 ns (FWHM). This magnitude of pulse length is accredited to cause very intense shock wave pressure due to bubble collapse in water [13, 16]. This 2.01-μm wavelength light source is a suitable tool to study the dependence of water composition in the calculus on fragmentation effectiveness due to its level of water absorption constant at 70 cm^{-1} [43].

2.1.4. Setup

Figure 9 shows the schematic diagram and picture of the hydrophone setup: (a) schematic block diagram; (b) pictures of the setup. From the schematic block diagram, the centerpiece is the blue color water tank that hosts three holders with 3-D adjustable stages,

http://dx.doi.org/10.5772/intechopen.69981

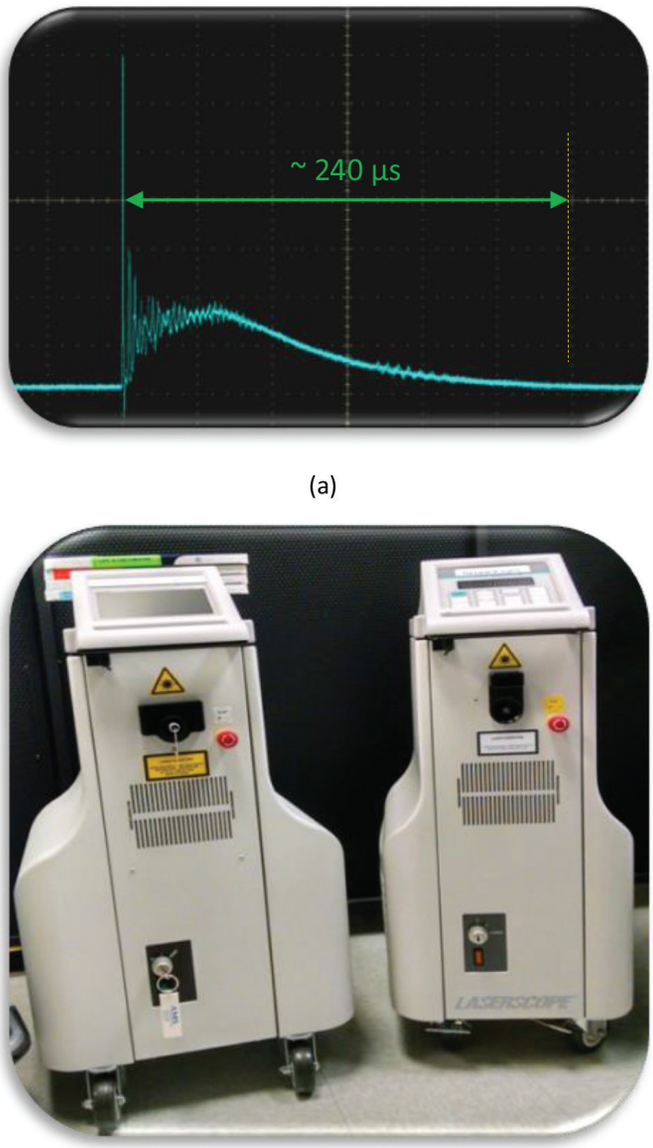

Figure 6. The StoneLight™ 30 Ho:YAG Laser system. (a) laser pulse trace; (b) Laser picture.

one for fiber (a 365-µm core diameter fiber, S-LLF365 SureFlex Fibre, Boston Scientific Corporation, San Jose, CA, USA, delivers the laser pulse), the second one for calculus phantom and the third one for the hydrophone (Mueller-Platte Needle Probe 100-100-1, Dr. Mueller Instruments, Germany). A ceramic screen is used to reflect the illumination from two high-intensity LED lamps for a better view of the action center near fiber tip. An SA5 camera from Photron (SA5 16G BW, Photron USA, Inc., San Diego, CA, USA), capable of one million frames per second, is used to record the event and the images are saved to the computer. The oscilloscope (Tektronix DPO 4140 Digital Phosphor Oscilloscope, Tektronix, Inc., Beaverton, OR, USA) is used to monitor and record the optical laser pulses detected by a photodetector (Thorlabs DET10D 2.6 µm InGaAs detector, Newton, NJ, USA) and the transient pressure signal from the hydrophone. In the hydrophone setup picture,

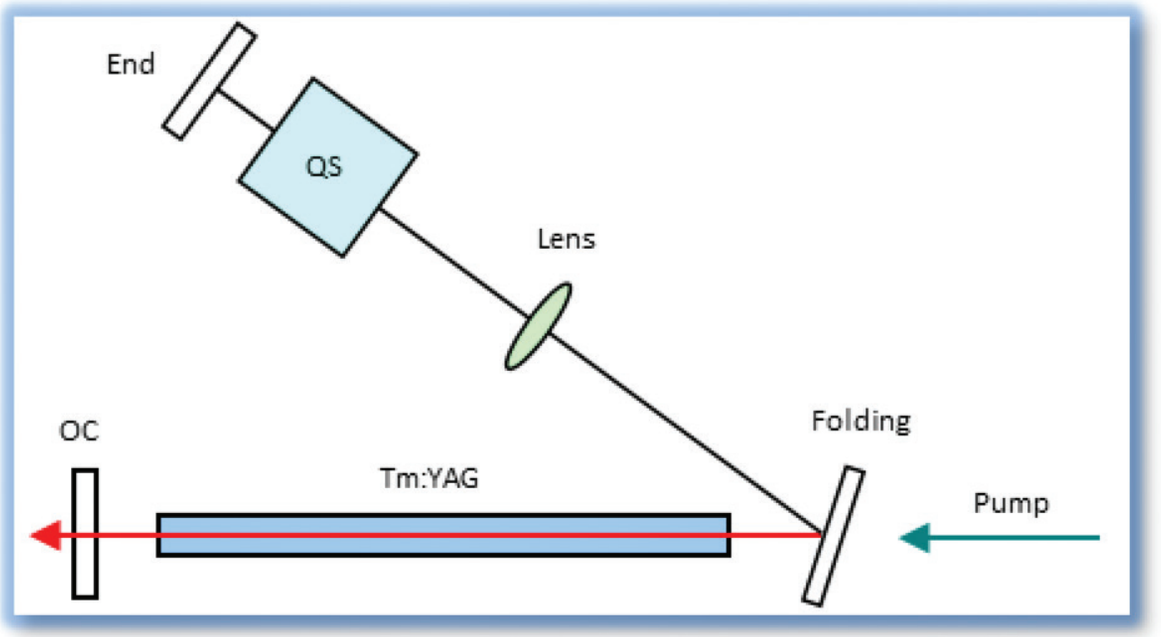

Figure 7. Lab built Q-switched Tm:YAG Laser setup.

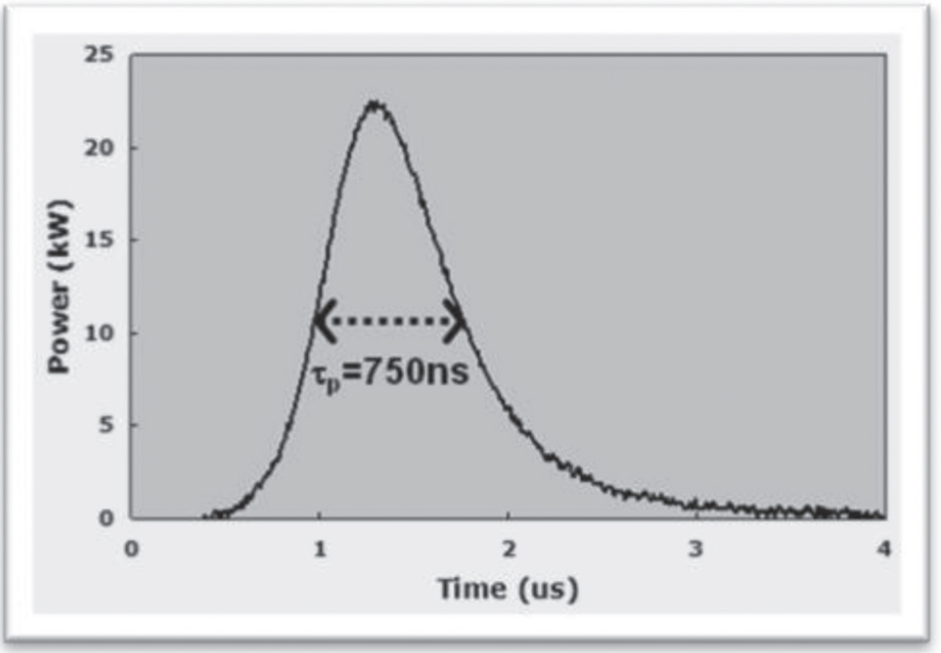

Figure 8. Q-switched Tm:YAG Laser Pulse.

it is shown that the tip of the hydrophone is ~10 mm away from the tip of the fiber. The hydrophone can be located at a different location or orientation if needed.

As a standard data collection convention, the entire test is repeated 10 times and each data point is an average of these 10 measurements.

http://dx.doi.org/10.5772/intechopen.69981

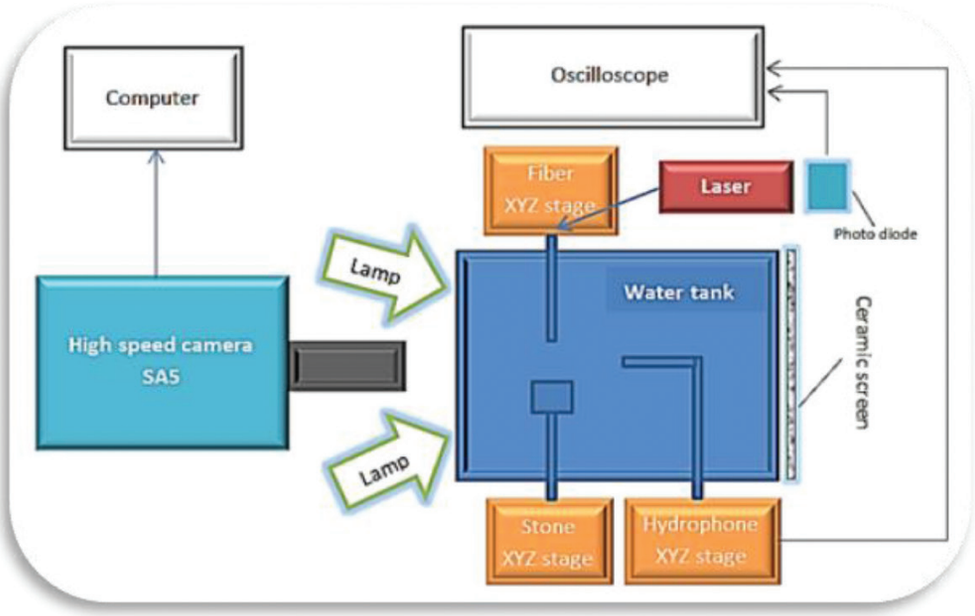

(a)

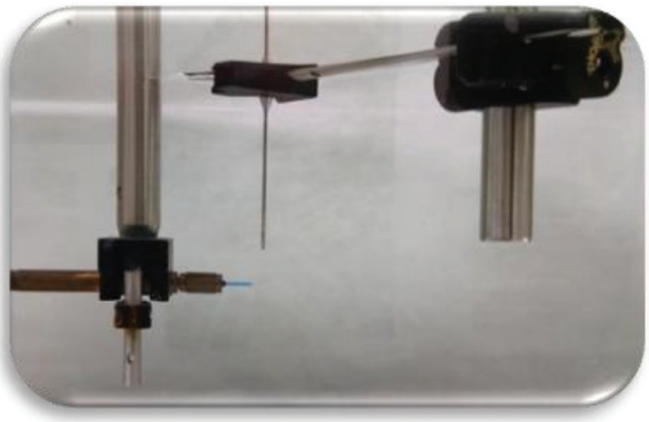

(b)

Figure 9. The schematic block diagram and pictures of the test setup. (a) Schematic block diagram; (b) Picture of the hydrophone setup.

2.2. Fiber-tip damage mechanism

2.2.1. Laser system

A commercially available Ho:YAG Lumenis VersaPulse® laser (VersaPulse® 100 W, Lumenis Ltd., Yokneam, Israel) was employed for this study. The laser is capable of generating 100 W of laser power at 50 Hz, and up to 3 J of pulse energy at 10 Hz. **Figure 3** shows a temporal pulse structure diagram of a typical 1-J pulse with a pulse duration (τ_p) of ~240 μs. Again, this magnitude of pulse duration is known to generate the photothermal effect necessary to fragment the stones [42].

This in vitro study again utilized a 365-μm core diameter fiber, and a calculus phantom (Plaster of Paris, 10 × 10 × 10 mm^3 cube) to mimic laser lithotripsy procedure. The test setup for laser-induced shock wave by the Schlieren imaging technique is depicted in **Figure 10**. The illuminating laser is a He-Ne beam at 543.5-nm wavelength. The two telescopes used for laser beam expansion each has a three times amplification. They enlarge the He-Ne beam size from ~1.7 to a 15 mm in diameter. The water box contains two handles with 3-D adjustable stages, one is for the fiber (a 365-μm core diameter fiber, S-LLF365 SureFlex Fibre, Boston Scientific Corp., San Jose, CA, USA) and the other is for the stone phantom. The focusing optics is a 100-mm plano-convex optics with a 2″ OD. The razor blade edge is positioned at the focus of the focusing optics. Besides, a high-speed camera was employed to videotape the laser-stone interaction. The SA5 camera from Photron has a frame rate of up to one million frames per second.

2.3. Calculus migration/retropulsion

2.3.1. Laser system

The laser system used for calculus migration/retropulsion is the same as that in Section 2.2.1.

2.3.2. Experimental setup

In this investigation, a commercial flash lamp pumped Ho:YAG laser at 2.13 μm, a 365-μm core diameter fiber, and a stone phantom (Plaster of Paris, 10 mm cube) were employed to simulate URS treatment process. An in-water pendulum is setup for recoil motion investigation, which

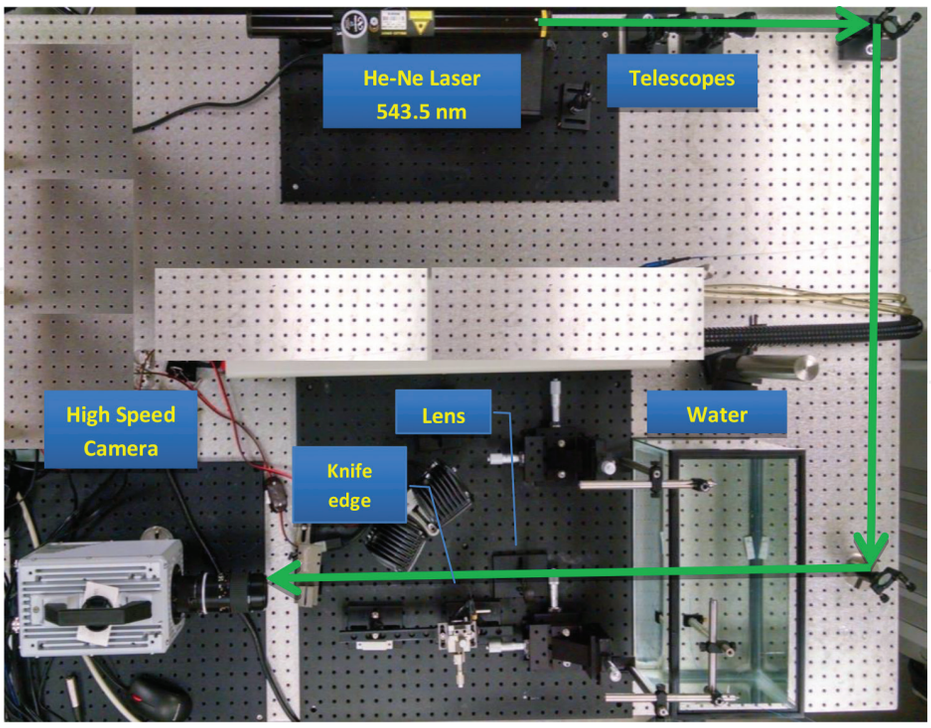

Figure 10. Schematic picture of test setup.

http://dx.doi.org/10.5772/intechopen.69981

is composed of a calculus phantom with the size of 10 × 10 × 10 mm^3 as depicted in **Figure 11**. The calculus phantom is hung underwater by a string of ~200-mm long. In order to control the rotational motion of the stone in case the laser pulse from the fiber is not exactly pointed at the center of the mass of the stone phantom, the stone is held in a clear plastic basket and two threads with a separation of ~10 mm are used to hang the phantom (**Figure 11b**). Since water has a relatively low viscosity (1.002 mPa*s), the suspended phantom pendulum under water has virtually no friction and is free to move in the direction perpendicular to the thread. A 365-μm core diameter fiber (S-LLF365 SureFlex Fibre, Boston Scientific Corp., San Jose, CA, USA) was used to deliver the laser pulse to the stone phantom. Furthermore, a high-speed camera was used to study the movement of the calculus. The SA5 camera from Photron (SA5 16G BW, Photron USA Inc., San Diego, CA, USA) is capable of one million frames per second as shown in **Figure 11(c)**. In contrast to a conventional camera, the high-speed camera can be used to video tape and to fully characterize the kinetic motion of the stone phantom retropulsion. These dynamic details include the displacement, speed, and acceleration parameters of the stone phantom during laser lithotripsy.

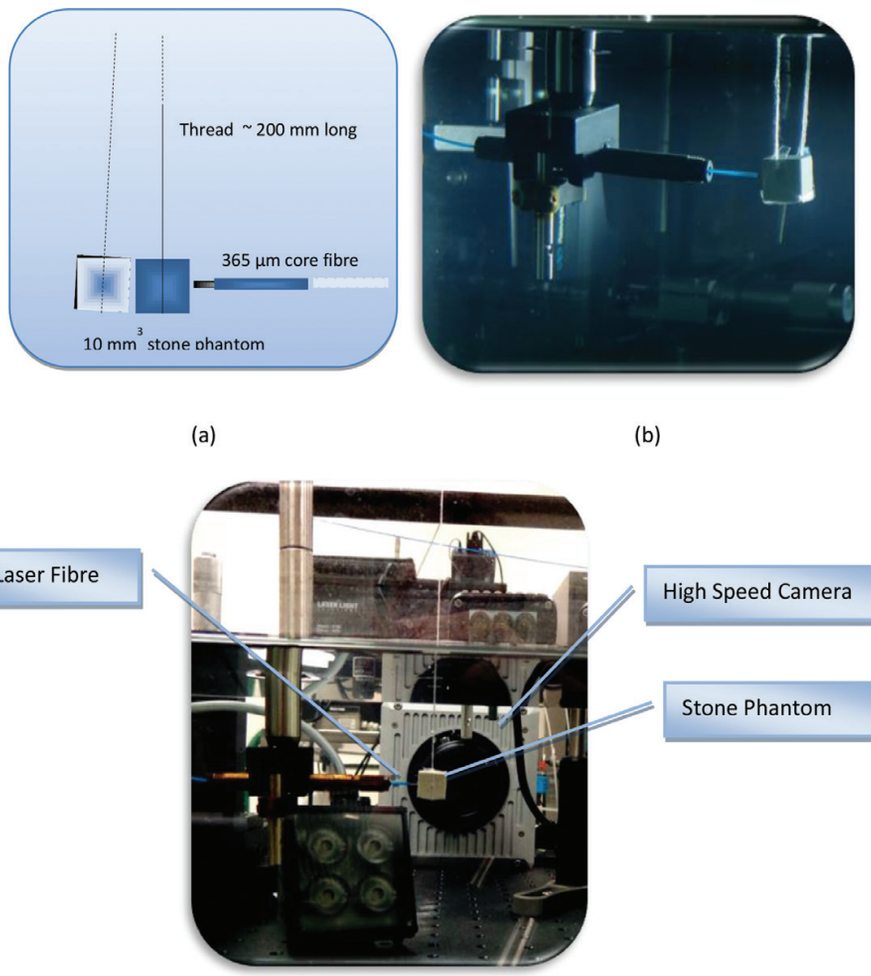

Figure 11. Schematic picture of the pendulum setup. (a) Schematic; (b) Picture of actual setup; (c) the experimental setup including the pendulum and high-speed camera.

3. Results

3.1. Cavitation bubble dynamics

3.1.1. Cavitation bubble dynamics in free running condition

The cavitation bubble dynamics was investigated by the aforementioned high-speed camera. **Figure 12** depicts a series of screen shots of cavitation bubble behavior created by the lasers. The Ho:YAG laser generated 1-J pulses with pulse widths of 150 and 800 μs. The Tm:YAG laser emitted 0.02-J pulse of a 450-ns duration. The high-speed camera SA5 was set at 300,000 fps with a viewing window of ~10.4 × 4.3 mm^2. As we can see from the pictures, the 150-μs pulse generates bubbles that oscillate up to ~3 times collapsing at 570, 773, and 902 μs. By contrast,

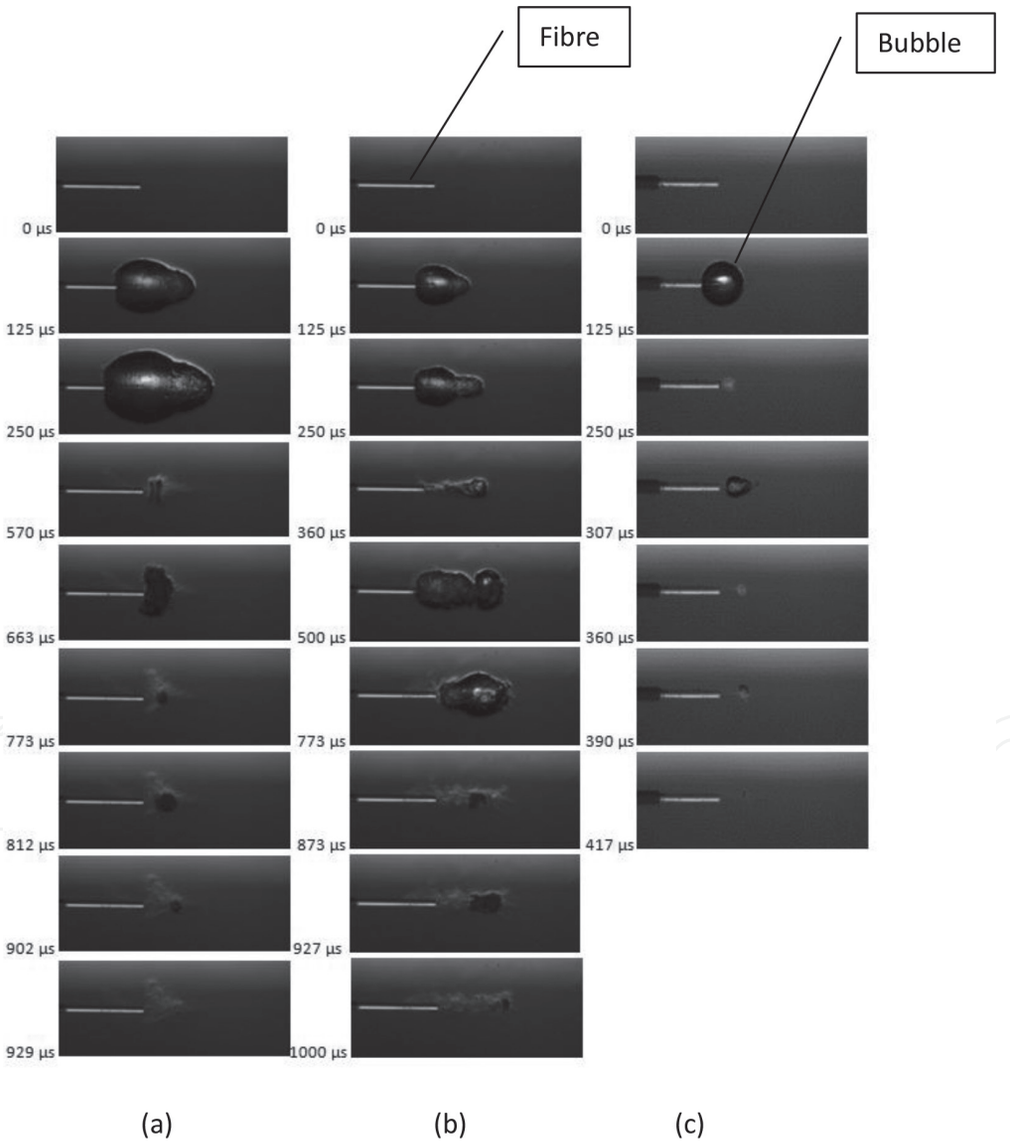

Figure 12. Series of screen shots of cavitation bubbles behavior of Ho and Tm lasers. (a) Ho at 1 J and 150 μs; (b) Ho at 1 J and 800 μs; (c) Tm 0.02 J and 450 ns.

http://dx.doi.org/10.5772/intechopen.69981

the 800-μs pulse has a smaller overall size, and the bubble appears to have two parts that oscillate at different frequencies (see the first burst of the left part of the bubble at ~360 μs). Furthermore, the center of the bubble moves further away from the fiber tip (see pictures ~800 and 1000 μs). The bubbles generated by the Q-switched Tm:YAG laser have a spherical shape, and the size is comparable to those generated by 800-μs 1-J Ho pulses. Like the bubbles generated by the 150-μs Ho:YAG pulse, those generated by the Tm:YAG laser can oscillate to up to ~3 times as a single bubble. However, the time to the first collapse is much shorter (~240 μs).

Figure 13 shows the cavitation bubble oscillation curves. Each data point indicates an average of 10 measurements, and the error bar depicts the standard deviation. **Figures 13(a)** and **(b)** represent the 1-J energy level for the Ho:YAG laser pulses. The length is the horizontal dimension of the bubble and the width is the vertical dimension of the bubble. The bubble's first collapse is at ~500 μs, while for the 0.02-J Tm:YAG Q-switched laser pulse in **Figure 13(c)**, the bubble's first collapse is at ~240 μs. **Figure 14** shows the cavitation bubble center movement

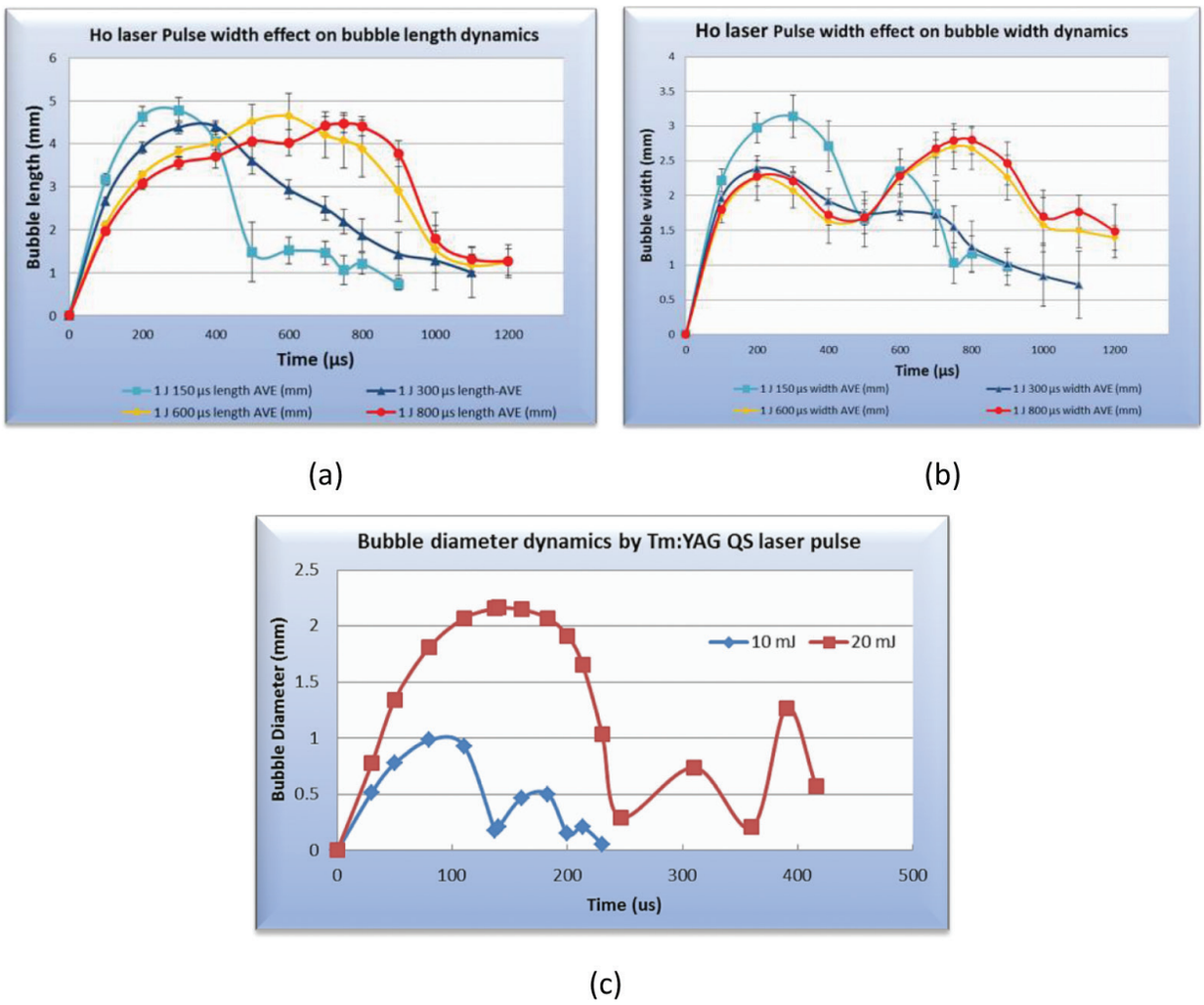

Figure 13. The cavitation bubble oscillation curves. (a) Bubble length oscillation curves of Ho:YAG 1 J laser pulse; (b) Bubble width oscillation curves of Ho:YAG 1 J laser pulse; (c) Bubble length/width oscillation curves of Tm:YAG 0.02 J laser pulse.

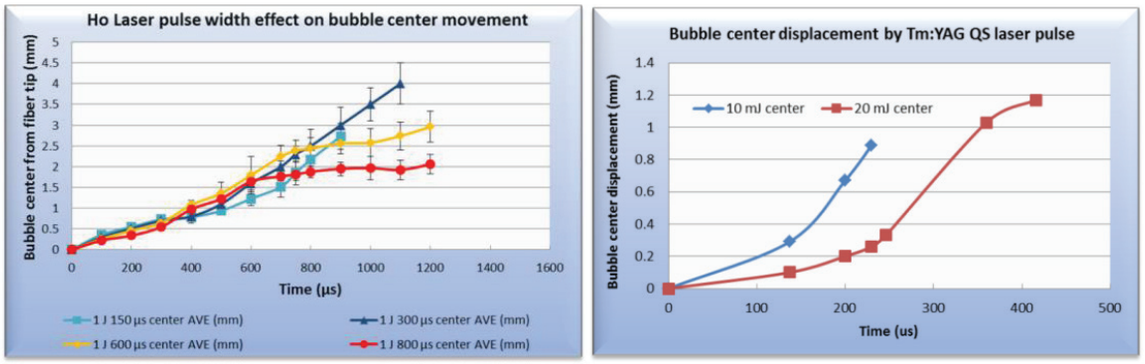

Figure 14. The cavitation bubble center movement at various laser pulse lengths. (a) Ho:YAG; (b) Tm:YAG.

at various laser pulse lengths. For the 1-J Ho:YAG laser pulse, at first bubble collapse of ~500 μs (this is typically the second and the highest transient pressure of the shock wave during the laser pulse interaction with the liquid fluid, while the first transient pressure of the shock wave is at the injection of the laser pulse as demonstrated in Section 3.1.3), Note that the bubble center is ~1 mm away from the tip of the fiber. By contrast, for the 0.02-J Tm:YAG Q-switched laser pulses, the first bubble collapse of ~240 μs, the bubble center is ~0.34 mm away from the tip of the fiber.

There is no observable difference of cavitation bubble dynamics between 273 and 365 μm fibers.

3.1.2. Dependency of cavitation bubble formation during lithotripsy on fiber-tip contact mode with the calculus surface

Next, we analyze the effect of contact mode whereby the fiber tip is in contact with the surface of the stone phantom. After analyzing the interaction video from the high-speed camera SA5 on the very first laser pulse hitting the stone, we observed bubble formation for both Ho:YAG and Tm:YAG laser pulses. However, in the Tm:YAG case, the bubbles can be seen more clearly because of much less debris generated by the 0.02-J pulse (as compared to the 50× stronger pulse in Ho:YAG laser case). The bubbles generated are hemispheres because of the existence of the stone phantom and the collapse time is shown in **Figure 15**. The bubble collapse time in contact mode is ~10–15% shorter as compared to the case without stone phantom contact for both Ho:YAG and Tm:YAG lasers.

3.1.3. Transient pressure level measurement

The transient pressure is measured by a hydrophone and its sensitivity $U_{probe} = Q_{probe}/C_{sum}$, where Q_{probe} is the 3.0 pC/MPa and C_{sum} is the sum of probe capacity including cable (244 + 13 = 257 pF); therefore, U_{probe} = 11.7 mV/MPa.

Figure 16 shows the oscilloscope traces of laser pulse and transient pressure. The upper picture has been created by a Ho laser pulse of 150 μs at 1 J and 10 Hz. The hydrophone end is

http://dx.doi.org/10.5772/intechopen.69981

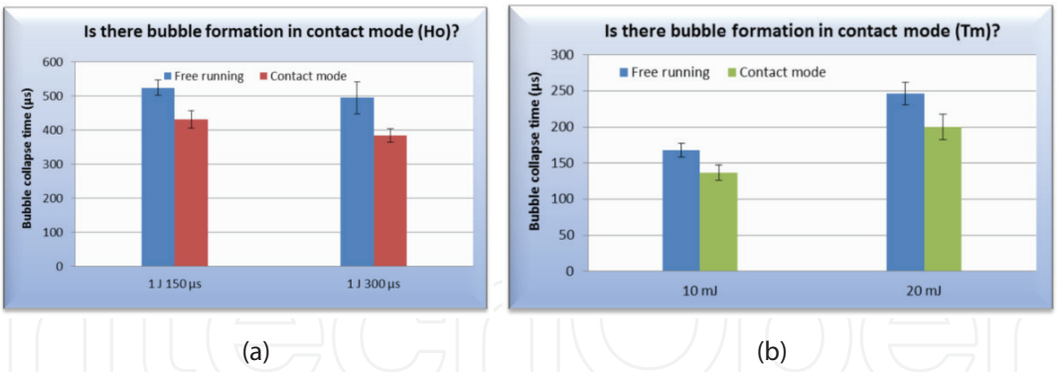

Figure 15. The cavitation bubble collapse time in contact mode. (a) Ho:YAG; (b) Tm:YAG.

positioned at ~10 mm from the fiber end to prevent the probe from any possible damage due to the laser beam or pressure wave. Because the rising period of the hydrophone sensor is 45 ns, the detected transient pressure may be less than the real value. The actual pressure curve (**Figure 16**) exhibits many spikes, the first of which commences immediately after the injection of the laser pulse. This first pulse in the time sequence (from the left) represents the first shock wave. The second or the highest transient pressure peak corresponds to the first collapse of the cavitation bubble at ~500 µs. The average transient pressure is ~18 mV or 1.5 MPa at 10 mm away from the fiber tip. In addition, the transient pressure resulting from a 1-J and 800-µs pulse is less than half of that of a 150-µs pulse.

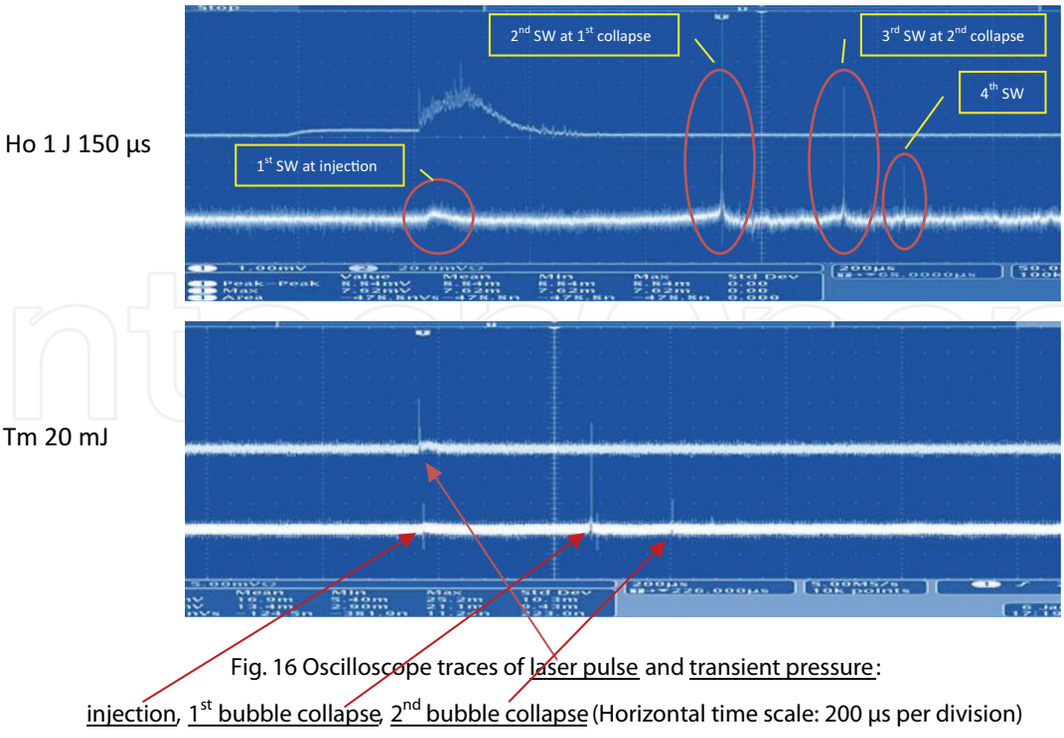

Figure 16. Oscilloscope traces of laser pulse and transient pressure: injection, first bubble collapse, second bubble collapse (horizontal timescale: 200-µs per division).

Similar sequences of transient pressure signals are shown in the lower picture, in which the first transient pressure by shock wave immediately after the injection of the laser pulse is more obvious, and the second transient pressure signal caused by bubble collapse at ~240 μs is again the strongest one. The highest transient pressure peak generated by a 20-mJ Tm:YAG Q-switched laser pulse is ~1.8 MPa at 10 mm from the fiber tip.

3.2. Fiber-tip damage mechanism

3.2.1. Shock wave detection

Shock waves generated by laser pulses are disturbance waves that travel faster than sound, but quickly damp down to the speed of sound [12]. The speed of sound under water is 1484 m/s or ~1.5 mm/μs; as such, a high-speed camera with a frequency of ~1 μs or 1 million fps is required for studying the dynamics of these pressure waves (with 930,000 fps, the period is ~1 μs, while the image size is barely a few mm wide).

Figure 17 shows a snapshot of the Schlieren image of shock wave by a 1-J pulse with a high-speed camera setting of 930,000 fps. In the picture, the captured image is at the moment when the shock wave (the area indicated in the middle) leaves the fiber-tip area and moves to the right.

Figure 18 depicts the shock-wave displacement curve against time. Utilizing a second-order polynomial curve fit, we can see the speed is 1.45 mm/μs or 1450 m/s. This is consistent with the sound speed in water (1484 m/s). However, the pressure wave is quicker than the acoustic velocity at the very beginning (within the 1-μs domain [12]). A well above 1-million fps frame rate camera is needed (best to be 10 million fps) so that a detailed understanding of the pressure wave initiated by Holmium laser energy can be obtained.

3.2.2. Fiber-tip damage

An additional set of tests were conducted on the thermal/mechanical damage to the fiber tip by debris by (1) varying the distance between the fiber tip and the calculus surface; (2) differing the incidence angle of the fiber to the calculus surface. According to a multicenter study of 541 procedures, the average dose of laser energy needed for laser lithotripsy is ~1.5 kJ [22]. Therefore,

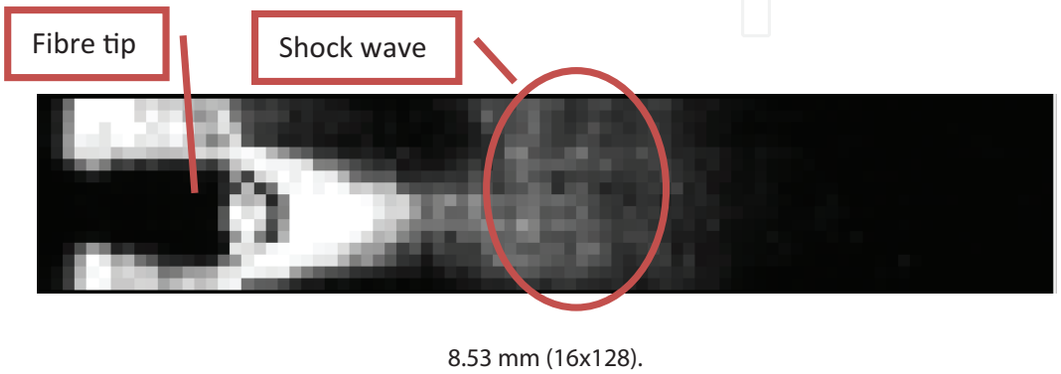

Figure 17. Shock-wave Schlieren image with a frame interval of 1.075 μs, and the frame size is 1.07 × 8.53 mm (16 × 128).

http://dx.doi.org/10.5772/intechopen.69981

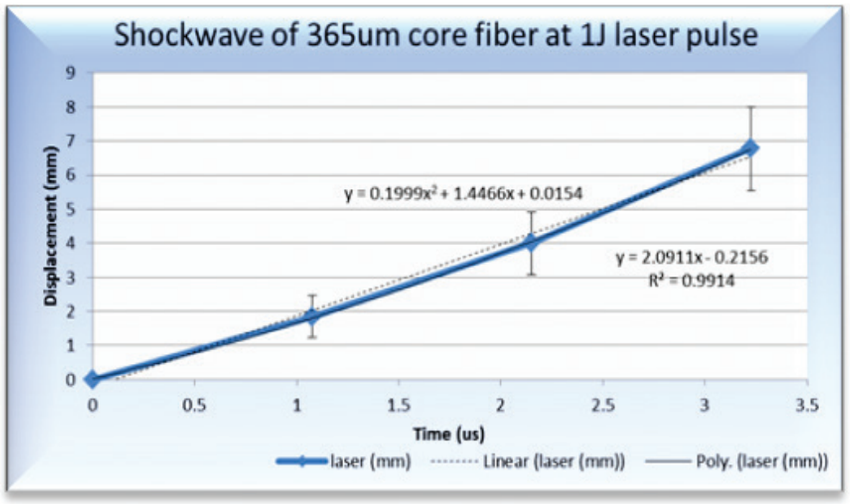

Figure 18. The shock-wave displacement curve against time.

a lasing time of 2.5 min (150 s) at 1 J and 10 Hz (which is equivalent of 1.5 kJ) is used for the damage tests shown subsequently.

Figure 19 shows images of the fiber and calculus with different incidence angles. In addition to varying the angular setting, the fiber tip is adjusted through a range of distances from the calculus (at 2, 1, 0.5, and 0 mm). Furthermore, the fiber is translated vertically at a velocity of ~0.4 mm/s within the 2.5-min laser on period in the same time holding a constant spacing from the phantom.

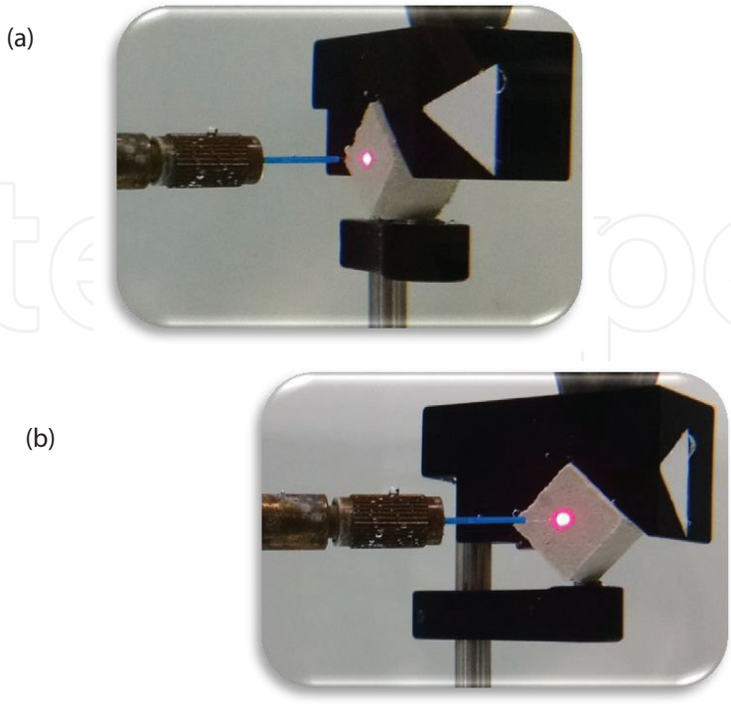

Figure 19. The images of fiber and stone phantom with various incidence angles. (a) 0° incidence; (b) 45° incidence.

In **Figure 20**, we show fiber-tip end views from fibers that underwent these various pulse conditions as well as an unused one. We utilized 1.5-kJ laser pulse trains at the four different fibers to calculus spacing (2, 1, 0.5, and 0 mm) and with two different incidence angles (0 and 45°). It is evident from the pictures that the fiber end surface damage/deformation becomes more severe as the separation between the fiber tip and calculus surface becomes smaller after 1.5 kJ of energy delivery. Besides, the 45° incidence angle results in less end surface damage/deformation verse 0° incidence angle for the same separation value. **Figure 21** depicts the transmission degradation of 365-μm fiber over working distance and an incidence angle after

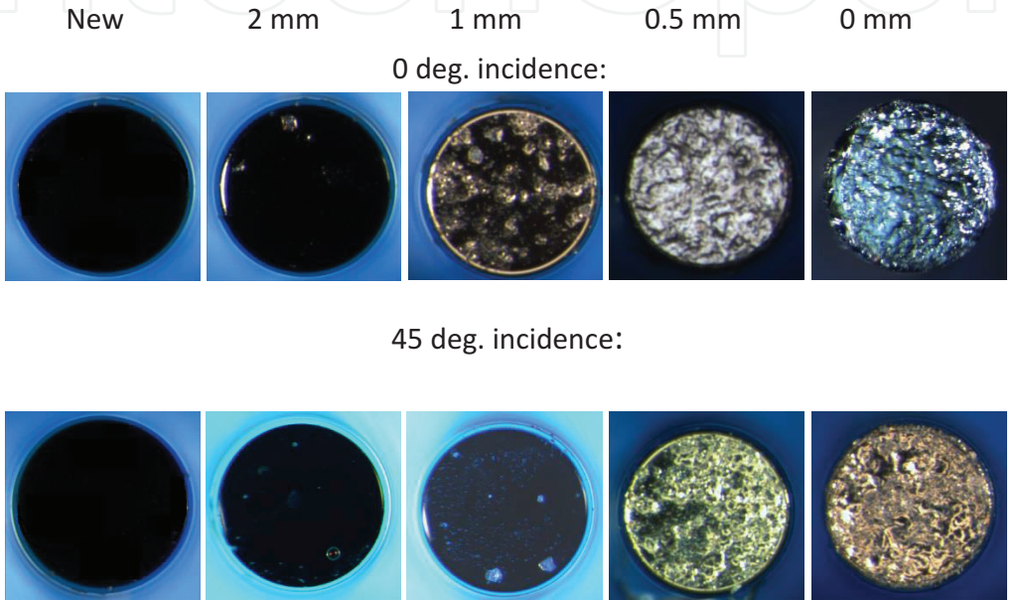

Figure 20. Fiber-tip end views from unused fibers in contrast to fibers after 1.5-kJ laser energy deliveries. Four different spacings (2, 1, 0.5, and 0 mm) between fiber tip and calculus surface, and with two different incidence angles (0 and 45°) were used for the activated fibers.

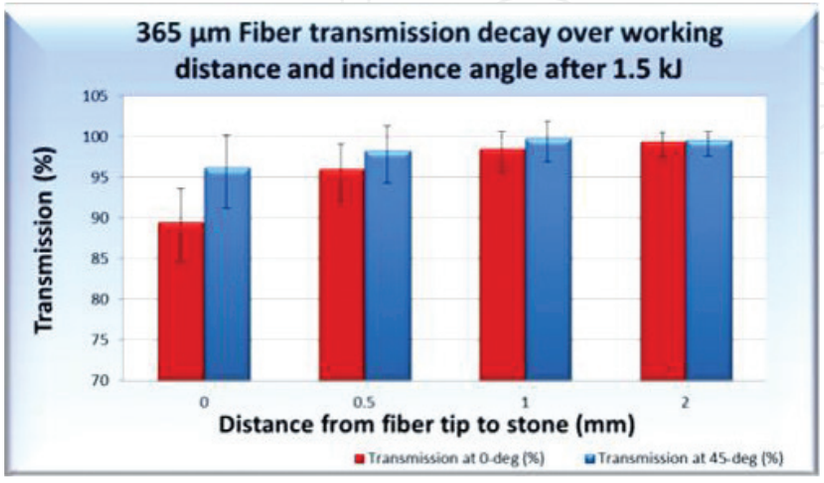

Figure 21. Transmission decay of a 365-μm fiber as a function of working distance and angle of incidence after 1.5 kJ of energy delivery.

1.5 kJ of energy delivery. The transmission measurement results are consistent with the surface damage/deformation results.

3.2.3. Retropulsion

Admittedly, our high-speed camera is capable of 1×10^6 fps, but the field of view is limited at rates greater than 7×10^3 fps. Therefore, we find that a frame rate of 1×10^4 fps is a good compromise between speed and field of view for our retropulsion study. For each measurement, the high-speed camera recorded 10,000 images during the 1-s interval of laser pulses interacting with the stone phantoms. Each measurement was repeated 5–10 times to improve the data quality. The video data files are analyzed using a MATLAB program. **Figure 22** shows the pendulum retropulsion test at a 10-kfps camera frame rate and utilizing a Ho:YAG laser delivering 0.5-J pulses at a repetition rate of 10 Hz. Hence, 10,000 data points are recorded at these conditions and are shown as a dotted curve. This dotted curve depicts the zero order of the motion and hence the displacement of the stone phantom. The apex of the movement occurs after ~0.83 s where the phantom reaches zero velocity and begins to swing back. From this zeroth-order curve, we can generate the first-order curve (shown in solid) which indicates the speed of the phantom. We note that the initial speed depicted in the curve is not zero. This is due to the inadequate resolution of the measurement system. At a frame rate of 1×10^4 fps, we have a 100-μs period between camera shots. This is too coarse compared to the 240-μs laser pulse since it will have a significant impact on the phantom within the 100-μs time frame. Lastly, the second-order motion represents the acceleration of the phantom and is represented by the Dotted-dash curve. The point that it crosses the zero acceleration line indicates the maximum speed of the phantom. Besides, the initial acceleration (multiplied by the phantom mass) is a good estimation of the average force that impacts on the pendulum by the laser pulse train within 1 s.

To further our study of retropulsion, we utilized our pendulum setup and employed various Holmium laser pulse energies impinging on a 200 mm–10 mm^3 stone phantom. In **Figure 23**, we show the maximum displacements of the stone phantom as a function of laser pulse energy. The increase of apex or maximum displacement with laser pulse energy is to be expected. The

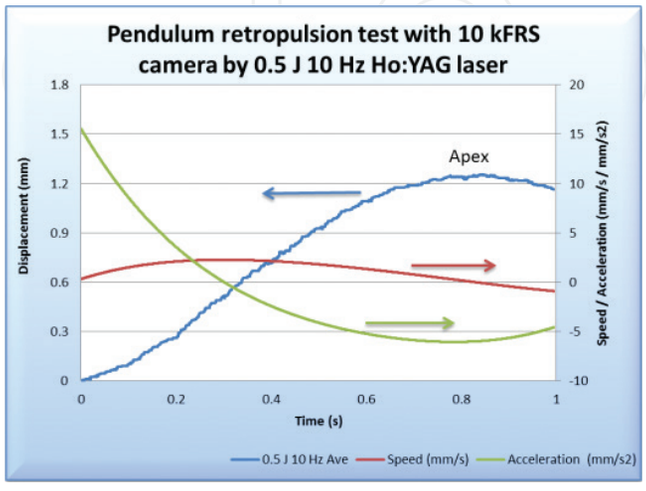

Figure 22. Pendulum retropulsion test with 10-kFRS camera by 0.5 J 10 Hz Ho:YAG laser.

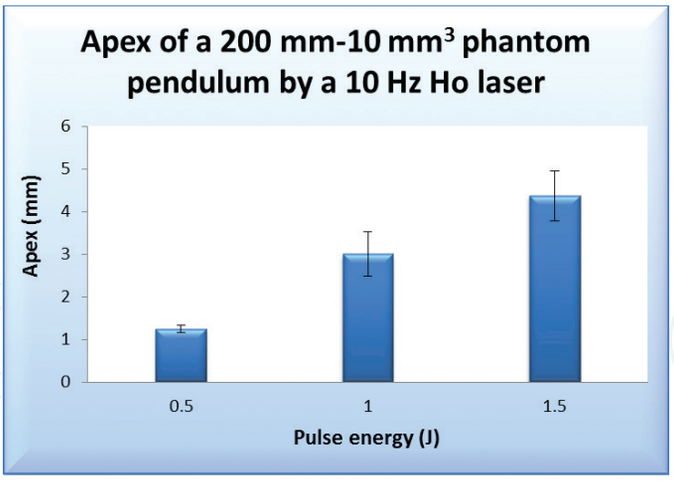

Figure 23. The apex of a 200 mm–10 mm^3 phantom pendulum by a 10-Hz Holmium laser.

results of displacement are 1.25 ± 0.10, 3.01 ± 0.52, and 4.37 ± 0.58 mm for 0.5, 1.0, and 1.5 J of energy per pulse, respectively.

From **Figure 22**, we can find out the initial acceleration of a 200 mm–10 mm^3 phantom pendulum by a 10-Hz Holmium laser at different pulse energy level. Taking into account the mass of the stone phantom ~2.0 g (wet and ~1.8 g when dry), the average initial force by 10 of the 0.5-J pulses is 3.1×10^{-5} Newton or 3.1 Dyne.

Figure 24 reveals the average power effect of retropulsion with the 0.5-J Holmium laser pulse train. Not surprisingly, the retropulsion increases with the average laser power applied. Apparently, the time to reach the apex increases with increasing average power. When the laser power level is increased above 25 W, the time for the phantom to come to the apex exceeds 1 s. This duration was beyond the high-speed camera recording time in our current study. In the future, further testing should be done with increased high-speed camera recording times (>1 s) to investigate the phantom dynamics at higher laser power levels.

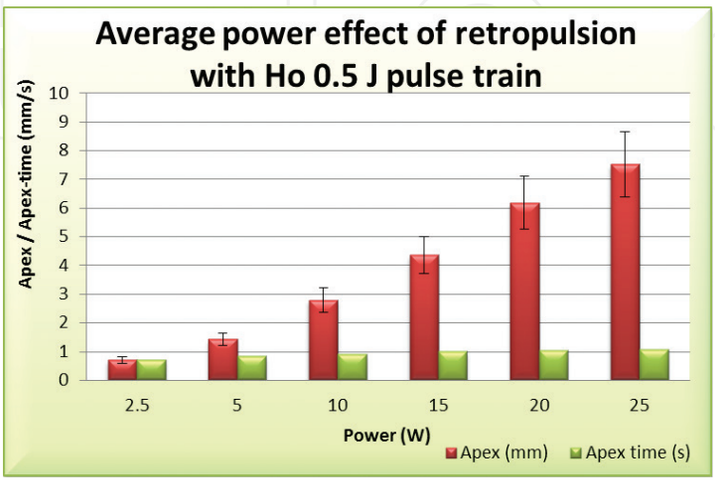

Figure 24. The average power effect of retropulsion with Holmium laser 0.5-J pulse train.

http://dx.doi.org/10.5772/intechopen.69981

4. Discussions

4.1. Cavitation bubble dynamics

Urinary calculi are crystalline deposits, also known as kidney/ureter/bladder/urethra stones or uroliths, which occur in the urinary system. The presence of urinary tract stones often causes the personal severe discomfort and pain. Even though laser lithotripsy has become the most popular treatment choice for kidney stone disease, the mechanism calculus disintegration by laser pulse remains unclear. This is due to the multiple physical/chemical processes involved in laser pulse-caused calculus damage and their sub-microsecond timescales. Cavitation bubble [9–16] dynamics are the centerpiece of the physical processes that link the whole energy flow chain from laser pulse to calculus damage.

In this study, cavitation bubble dynamics was investigated by a high-speed camera and a needle hydrophone. We keep the following three questions in mind when performing the investigation:

1. What are the differences in the characteristics of the bubble dynamics when utilizing short pulses versus long pulses emitted from a Ho:YAG laser?
2. Is a cavitation bubble formed during lithotripsy when the fiber tip is in contact mode with the surface of the calculus?
3. What are the characteristics of the bubble dynamics for a Q-switched Tm:YAG laser [18, 19] in reference to the benchmark Ho:YAG laser lithotripter?

The results revealed the following:

1. The cavitation bubbles generated when utilizing long pulses have a smaller overall size (less transient pressure) and appear to have two parts that oscillate at different frequencies. The two bubbles are observed in **Figure 12(b)** wherein the first burst of the left part of the bubble is evident at ~360 μs and the center of the bubble moves further away from the fiber tip (action center shifting). We also observed that the transient pressure generated by a 1-J and 800-μs pulse is less than half of that of a 1-J and 150-μs pulse.
2. Bubbles are formed even when the fiber tip is in contact with the stone. The bubbles generated in contact mode are hemispheres because of the presence of the stone phantom. It was noted that the bubble collapse time in contact mode is ~10–15% shorter as compared to the noncontact cases for both Ho:YAG and Tm:YAG lasers.
3. The cavitation bubbles generated from the Ho:YAG laser pulses exhibited a football shape. By contrast, those generated by the Q-switched Tm:YAG (20-mJ) laser pulses were perfectly spherical. The size of the Tm:YAG produced bubbles is comparable to those of the 1 J at 800-μs Ho:YAG pulses. However, the time to the first collapse is much shorter (~240 μs) for the Tm:YAG bubbles and they can oscillate up to approximately three times as a single bubble. The highest transient pressure peak observed for the 20-mJ Tm:YAG Q-switched laser pulses was ~1.8 MPa at 10 mm from the fiber tip. This is similar to the peak pressure observed for 1 J at 150-μs Ho:YAG pulses.

The transient pressure trace by a hydrophone located ~10 mm away from the fiber tip reveals that the first shock wave appears immediately after the injection of the laser pulse. However, the second and the highest transient pressure peak corresponds to the first collapse of the cavitation bubble as shown in **Figure 16**. Since pressure peak can be much larger than the magnitude of the first shock wave, the latter is often overlooked. It should be noted that the first shock wave is more evident (higher peak pressure) at high laser pulse energies or short-pulse widths as present in the Tm:YAG laser case.

Finally, we observed no discernible difference of cavitation bubble dynamics when switching between 273- and 365-μm core fibers. This is most likely because the cavitation bubble dynamics relates more to the pulse energy and pulse width, as opposed to the pulse intensity. A more detailed investigation of the relationship between cavitation bubble dynamics and calculus damage (fragmentation/dusting) will be conducted as a future study.

4.2. Fiber-tip damage mechanism

Admittedly, a retrospective study in Ref. [6] revealed superior stone-free rates results for renal stones <1.5 cm for URS compared with SWL. However, the fibers used in URS as energy delivery devices often suffer distal-end damage. This is usually referred as fiber-end burn-back [20–23]. Fiber-tip burn-back results in a reduced transmission of laser energy, which significantly reduces the efficiency of stone comminution. Though it is known that the higher the energy fluence (which is the ratio of the laser energy over the cross-section area of the fiber core), the faster the fiber-tip degradation, the damage mechanism of the fiber tip is still unclear.

In this study, fiber-tip degradation was investigated by the visualization of shock wave, cavitation/bubble dynamics, and calculus debris ejection with a high-speed camera and the Schlieren method. The primary chromophore of 2.01-μm Holmium laser is water, which is critical for fragmentation of the calculus during laser lithotripsy [19]. The shock wave [9, 10, 12–14] that the laser pulse generated is a disturbance wave that is faster than a sound wave. Because of the transparency of water liquid, pressure wave imaging inside water is not as straightforward. However, the Schlieren method can reveal the acoustic wave inside water [15], just like an X-ray which can reveal the invisible pressure variation inside a transparent matter.

Laser energy-induced shock wave, cavitation/bubble dynamics, and stone debris ejection were recorded by a high-speed camera with a frame rate of 10,000–930,000 fps. The shock wave is successfully detected using the Schlieren imaging technique. The results suggested that using a high-speed camera and the Schlieren method to visualize the shock wave provided valuable information about time-dependent acoustic energy propagation and its interaction with cavitation and calculus. We successfully observed the shock wave generated immediately after the injection of the laser pulse. This "first" shock wave was also detected by a transient pressure sensor (hydrophone) as discussed in Section 3.1.3. By plotting the shock-wave displacement curve against time, we revealed that the acoustic wave speed that was more than 1 mm away from the fiber tip was 1.45 mm/μs or 1450 m/s. This is comparable to the sound speed in water (1484 m/s). Furthermore, it is in good agreement with Ref. [12] that indicates shock waves only exist within a millimeter of the fiber tip and

travel faster than the sound speed. Therefore, in the current study that utilized a high-speed camera with a frame rate of 1 million fps, or 1 μs per frame, the acoustic wave will travel 1.48 mm during a camera frame. Apparently, a high-speed camera with frame rate well at or near 10 million fps is desired to resolve more detail of the shock-wave dynamics generated by laser pulses.

The role of debris in fiber-tip damage is also studied. Fiber-tip damage/degradation/burn-back mechanism is an intricate subject due to its numerous physical phenomena, for example, sonic shock waves, self-focusing of the laser beam, and transient thermal surge, and so on. It covers three areas of degradation mechanisms:

1. Mechanical: shock wave and debris impulsion;
2. Thermal: heating/liquidating of material, transient thermal surge because of the absorption of self-focusing laser beam by the microstructure of the fiber-tip surface material;
3. Optical: photoionization or plasma [24].

The function of the stone particle in fiber-tip degradation mechanism has two folds: kinetic impulsion and thermal heating/melting. **Figure 25** depicts the stone particle clusters hovering around the fiber-end area and the fiber-end degradation/deformation after 1.5-kJ laser power dose and laser-stone interaction in our test. Our investigation reveals that the fiber-tip degradation/deformation is more significant when the spacing between the fiber end and stone surface is less. And with similar spacing, the 45° incidence angle leads to less tip surface degradation/deformation as compared to 0° incidence ones.

More investigation should be performed to find out the predominant degradation mechanism by the stone particle (thermal or kinetic), cavitation bubble dynamics, and balance between degradation/burn-back control and the stone dusting efficiency.

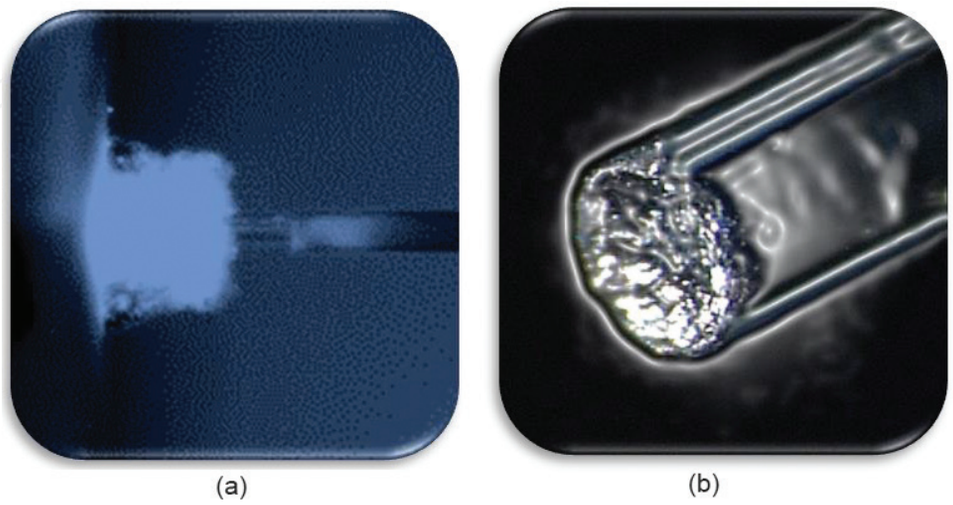

Figure 25. The stone particle clusters hovering around the fiber-end area (a) and the fiber-end degradation/deformation after 1.5-kJ laser power dose and laser-stone interaction (b).

4.3. Calculus migration/retropulsion

A few investigations of the URS treatment of upper ureteral calculi have revealed that the main reason for calculus-free failures can be due to recoil motion and less frequently to inability to track or seek the stones [35–37]. Recoil-dislocated calculus could lead to longer operation period, the necessity for another process to deal with recoiled parts and as such reduced stone-free level. The stone recoil motion results in additional patient morbidity and healthcare expenses [30, 33]. Besides, left-behind stone debris can act as a seed for calculus growing back, renal colic, and persistent infection.

Recoil motion investigations in the past revealed the relation between retropulsion displacement and laser power, frequency, and fiber core size [28–31]. Recoil motion is proportional to the laser power and the fiber core size. Furthermore, another research claimed that the recoil motion decreased with a longer laser pulse without compromising dusting effectiveness significantly [32]. A conventional experimental method to characterize calculus migration utilized a hosting container (e.g., a "V" groove, a flat and smooth surface, or a test tube). These methods, however, demonstrated large variation and poor detectability, possibly attributing to friction between the calculus and the container on which the calculus was situated. Our earlier study of retropulsion [38] and Blackmon et al. [44] showed more than 100% the peak-to-peak retropulsion variation with the conventional experimental method.

Sroka et al. [39] used a ball-shaped lead sinker fixed to a nylon string to study the retropulsion during laser lithotripsy with a regular CCD camera. In this in vitro study, a high-speed camera was used to study the movement of the calculus which covered displacement, speed, and acceleration. Our study shows that the combination of a pendulum and a high-speed camera provides a very useful tool for retropulsion characterization. The apexes of a 200 mm–10 mm^3 phantom pendulum by a 10-Hz Holmium laser are 1.25 ± 0.10, 3.01 ± 0.52, and 4.37 ± 0.58 mm for 0.5-, 1.0-, and 1.5-J energy per pulse, respectively (peak-to-peak variation is less than 50%). And the average initial force by 10 of 0.5-J pulses is 3.1×10^{-5} Newton or 3.1 Dyne. These data conclude that utilizing a pendulum method to get rid of the friction enhanced the detectability and repeatability, and the high-speed camera provides a better understanding of laser-calculus interaction, especially the recoil motion of the calculus and its particles, cavitation bubble forming and burst, and so on.

Even though URS is now the top treatment choice for urolithiasis, further investigation should be done to gain a thorough knowledge of the detailed processes during the laser-water and laser-stone interactions. At least four processes play a role in the URS: (1) heat (super-heated water or sometimes plasma formation); (2) acoustic or pressure wave (cavitation bubble forming and burst); (3) chemical (disintegrate of mechanical and chemical bond between the calculus particles); (4) physical kinetic (recoil motion of the calculus and scattering of the particles). The high-speed camera combined with a calculus pendulum can provide a better understanding of items 2 and 4. More investigation should be conducted on all of the four processes of the laser-calculus interactions in the URS.

In summary, combining a high-speed camera with other tools/method: hydrophone, pendulum, and Schlieren imaging method, provides not only a very useful tool for cavitation bubble, shock wave, fiber burn-back, and retropulsion characterization but also a great insight into laser-calculus interaction in regard to acoustic and kinetic processes.

Acknowledgements

The authors thank Jason Gong, Xirong Yang, and Joanne Banuelos of Boston Scientific Corporation for their assistance with preparing the Tm:YAG Q-switched laser and tissue phantoms. Besides, we thank David Jebens of Boston Scientific Corporation for his help in capturing the fiber-tip images using Leica M205C Stereo Microscope. Final thanks extend to Grant Getzan of Boston Scientific Corporation for his assistance with the experiments.

Author details

Jian J. Zhang*, Rongwei J. Xuan and Thomas Hasenberg

*Address all correspondence to: james.zhang@bsci.com

Boston Scientific Corporation, San Jose, California, USA

References

[1] Matlaga BR, Jansen JP, Meckley LM, Byrne TW, Lingeman JE. Economic outcomes of treatment for ureteral and renal stones: A systematic literature review. Journal of Urology. 2012;**188**(8):449-454

[2] Rizvi SAH, Naqvi SAA, Hussain Z, Hashmi A, Hussain M, Zafar MN, Mehdi H, Khalid R. The management of stone disease. BJU International. 2002;**89**(Supplement 1):62-68

[3] Tiselius H-G. Epidemiology and medical management of stone disease. BJU International. 2003;**91**:758-767

[4] Pearle MS, Calhoun EA, Curhan GC. Urologic Diseases of America Project. Urologic diseases in America project: Urolithiasis. Journal of Urology. 2005;**173**:848-857

[5] Stephan Seklehner Meliswa A, Del Pizzo LJ, Chughtai B, Lee RK. Renal calculi: Trends in the utilization of shockwave lithotripsy and ureteroscopy. The Canadian Journal of Urology. 2015;**22**(1):7627-7634

[6] Cone EB, Eisner BH, Ursiny M, Pareek G. Cost-effectiveness comparison of renal calculi treated with ureteroscopic laser lithotripsy versus shockwave lithotripsy. Journal of Endourology. 2014;**28**(6):639-643

[7] Zhang JJ, Xuan JR, Yu H, Devincentis D. Study of cavitation bubble dynamics during Ho:YAG laser lithotripsy by high-speed camera. In: Proceedings of SPIE. Vol. **9689**. Photonic Therapeutics and Diagnostics XII. 96891E. San Francisco, California, USA: SPIE; 2016. P. 1-7

[8] Zhang JJ, Rajabhandharaks D, Xuan JR, Chia RWJ, Hasenberg T. Characterization of calculus migration during Ho:YAG laser lithotripsy by high speed camera using

suspended pendulum method. In: Proceedings of SPIE. Vol. **8926**. Photonic Therapeutics and Diagnostics X. 89261I. San Francisco, California, USA: SPIE; 2014. P. 1-7

[9] Akhatov I, Lindau O, Topolnikov A, Mettin R, Vakhitova N, Lauterborn W. Collapse and rebound of a laser-induced cavitation bubble. Physics of Fluids. 2002;**13**(10):2805-2819

[10] Johnsena E, Colonius T. Shock-induced collapse of a gas bubble in shockwave lithotripsy. Journal of Acoustic Society of America. 2008;**124**(4):2011-2020

[11] Zhang JJ, Getzan G, Xuan JR, Yu H. Study of fibre-tip damage mechanism during Ho:YAG laser lithotripsy by high-speed camera and the Schlieren method. In: Proceedings of SPIE. Vol. **9303.** Photonic Therapeutics and Diagnostics XI. 930311. San Francisco, California, USA: SPIE; 2015. P. 1-10

[12] Lauterborn W, Vogel A. shockwave emission by laser generated bubbles. In: Delale CF, editor. Bubble Dynamics & Shock Waves. Springer-Verlag; Shockwaves. 2013;**8**:67-103

[13] Zhong P, Tong H-L, Cocks FH, Pearle MS, Preminger GM. Transient cavitation and acoustic emission produced by different laser lithotripters. Journal of Endourology. 1998;**12**(4):371-378

[14] Lee H, Gojani AB, Han T-H, Yoh JJ. Dynamics of laser-induced bubble collapse visualized by time-resolved optical shadowgraph. Journal of Vision. 2011;**14**:331-337

[15] Korpel A, Mehrl D, Lin HH. Schlieren imaging of sound fields. In: IEEE 1987 Ultrasonics Symposium. Denver, Colorado, USA: IEEE; 1987. p.515-518

[16] Jansen ED, Asshauer T, Frenz M, Motamedi M, Delacretaz G, Welch AJ. Effect of pulse duration on bubble formation and laser-induced pressure waves during Holmium laser ablation. Lasers in Surgery and Medicine. 1996;**18**(3):278-293

[17] Sroka R, Pongratz T, Scheib G, Khoder W, Stief CG, Herrmann T, Nagele U, Bader MJ. Impact of pulse duration on Ho:YAG laser lithotripsy: Treatment aspects on the single-pulse level. World Journal of Urology. 2015;**33**:479-485

[18] Zhang JJ, Rajabhandharaks D, Xuan JR, Wang H, Chia RWJ, Hasenberg T, Kang HW. Water content contribution in calculus phantomablation during Q-switched Tm:YAG laser lithotripsy. Journal of Biomedical Optics. 2015;**20**(12):128001

[19] Rajabhandharaks D, Zhang JJ, Wang H, Xuan JR, Chia RWJ, Hasenberg T, Kang HW. Dependence of water content in calculus phantom during Q-switched Tm:YAG laser lithotripsy. In: Proceedings of SPIE. Vol. 8565. Photonic Therapeutics and Diagnostics IX. 856519. San Francisco, California, USA: SPIE; 2013.

[20] Mues AC, Teichman JMH, Knudsen BE, FRCSC. Quantification of Holmium:Yttrium aluminum garnet optical tip degradation. Journal of Endourology. 2009;**23**(9):1425-1428

[21] Marks AJ, Mues AC, Knudsen BE, Teichman JMH. Holmium:Yttrium-aluminum-garnet lithotripsy proximal fibre failures from laser and fibre mismatch. Urology. 2008;**71**(6): 1049-1051

[22] Knudsen BE, Pedro R, Hinck B, Monga M. Durability of reusable holmium:YAG laser fibres: A multicenter study. The Journal of Urology. 2011;**185**:160-163

[23] Patel AP, Knudsen BE. Optimizing use of the Holmium:YAG laser for surgical management of urinary lithiasis. Current Urology Reports. 2014;**15**:397-404

[24] Manenkov AA. Fundamental mechanisms of laser-induced damage in optical materials: Today's state of understanding and problems. Optical Engineering. 2014;**53**(1):010901-1-7

[25] Kang HW, Lee H, Teichman JM, Oh J, Kim J, Welch AJ. Dependence of calculus retropulsion on pulse duration during Ho: YAG laser lithotripsy. Lasers in Surgery and Medicine. 2006;**38**:762-772

[26] Kuznetsov LI. Recoil momentum at a solid surface during developed laser ablation. Quantum Electronics. 1993;**23**:1035-1038

[27] Foth HJ, Meyer D, Stockel T. Side effects of laser tissue interaction studied by laser Doppler vibrometry. Proceedings of SPIE. 2000;**4072**:392-400

[28] White MD, Moran ME, Calvano CJ, Borhan-Manesh A, Mehlhaff BA. Evaluation of retropulsion caused by Holmium:YAG laser with various power settings and fibres. Journal of Endourology. 1998;12:183-186

[29] Lee H, Ryan RT, Kim JH, Choi B, Arakeri NV, Teichman JMH, Welch A. Dependence of calculus retropulsion dynamics on fiber size and radiant exposure during Ho:YAG lithotripsy. Journal of Biomedical Engineering. 2004;**126**:507-515

[30] Eisner BH, Pengune W, Stoller ML. Use of an antiretropulsion device to prevent stone retropulsion significantly increases the efficiency of pneumatic lithotripsy: An in vitro study. BM International 2009;**104**:858-861

[31] Robinson M, Teichman JMH. Laser lithotripsy retropulsion varies with stone mass. European Urology Supplements. 2013;**12**:e1063

[32] Finley DS, Petersen J, Abdelshehid C, Ahlering M, Chou D, Borin J, Eichel L, McDougall E, Clayman RV. Effect of Holmium:YAG laser pulse width on lithotripsy retropulsion in vitro. Journal of Endourology. 2005;**19**:1041-1044

[33] Lee HJ, Box GN, Abraham JB, Deane LA, Elchico ER, Eisner BFI, McDougall EM, Clayman RV. In vitro evaluation of nitinol urological retrieval coil and ureteral occlusion device: Retropulsion and Holmium laser fragmentation efficiency. Journal of Urology. 2008;**180**(3):969-973

[34] Marguet CG, Sung IC, Springhart WP, L'Esperance JO, Zhou S, Zhong P, Albala DM, Preminger GM. In vitro comparison of stone retropulsion and fragmentation of the frequency doubled, double pulse Nd:YAG laser and the Holmium:YAG laser. Journal of Urology. 2005;**173**(5):1797-1800

[35] Safer M, Watterson JD, Wollin TA, Nott L, Razvi H. Denstedt JD. Holmium:YAG laser lithotripsy for upper urinary tract calculi in 598 patients. Journal of Urology. 2002;**167**(1):31-34

[36] Cheung MC, Lee F, Yip SK, Tarn PC. Outpatient Holmium laser lithotripsy using semi-rigid ureteroscope. Is the treatment outcome affected by stone load? European Urology. 2001;**39**(6):702-708

[37] Lee Ryan RT, Teichman JM, Kim J, Choi B, Arakeri NV. Welch AJ Stone retropulsion during Holmium:YAG lithotripsy. Journal of Urology. 2003;**169**(3):88I-885

[38] Rajabhandharaks D, Kang HW. Short-pulsed Tm:YAG laser lithotripsy: Comparative study on ablation performance with conventional Ho: YAG laser. In: SPIE Photonics West BIOS Conference 8207B-47, Session 4: Therapeutics and Diagnostics in Urology: Lasers, Robotics, Minimally Invasive, and Advanced Biomedical Devices. San Francisco, California, USA: SPIE; 2012.

[39] Sroka R, Haseke N, Pongratz T, Hecht V, Tilld D, Stief CG, Bader MJ. In vitro investigations of repulsion during laser lithotripsy using a pendulum set-up. Lasers in Medical Science. 2012;**27**:637-643

[40] Carey RI, Kyle CC, Carey DL, Leveillee RJ. Preparation of artificial kidney stones of reproducible size, shape, and mass by precision injection molding. Journal of Endourology. 2008;**22**(1):127-131

[41] Delvecchio FC, Auge BK, Brizuela RM, Weizer AZ, Zhong P, Preminger GM. In vitro analysis of stone fragmentation ability of the FREDDY Laser. Journal of Endourology. 2004;**17**(3):177-179

[42] Vassar GJ, Chan KF, Teichman JMH, Glickman RD, Weintraub ST, Pfefer TJ, Welch AJ. Holmium:YAG lithotripsy: Photothermal mechanism. Journal of Endourology. 1999;**13**(3): 181-190

[43] Wieliczka David M, Shengshan W, Querry Marvin R. Wedge shaped cell for highly absorbent liquids: Infrared optical constants of water. Applied Optics. 1989;**28**(9): 1714-1719

[44] Blackmon RL, Irby PB, Fried NM. Comparison of Holmium:YAG and thulium fibre laserlithotripsy: Ablation thresholds, ablation rates, and retropulsion effects. Journal of Biomedical Optics. 2011;**16**:071403